02

Generation of terahertz radiation by multiple pseudomorphic quantum wells {InGaAs/InAlAs} with orientations (100) and (111)A

© E.A. Klimov[1,2], S.S. Pushkarev[1], A.N. Klochkov[3], P.M. Kovaleva[4], K.A. Kuznetsov[4]

[1] National Research Center „Kurchatov Institute“, Moscow, Russia
[2] Joint Stock Company NPO „Orion“, Moscow, Russia
[3] National Research Nuclear University „MEPhI“, Moscow, Russia
[4] Department of Physics, Moscow State University, Moscow, Russia

e-mail: s_s_e_r_p@mail.ru

Received December 05, 2024
Revised December 09, 2024
Accepted December 10, 2024

The influence of the built-in electric field in heterostructures on the generation of terahertz (THz) radiation under femtosecond laser pumping of the heterostructure surfaces has been investigated. The heterostructures consist of elastically strained superlattices of $\{In_{0.53+\Delta x}Ga_{0.47-\Delta x}As/In_{0.52-\Delta x}Al_{0.48+\Delta x}As\}$, epitaxially grown on InP substrates with (100) and (111)A orientations. The value of Δx, and hence the value of strain, varied in series of samples. The „red“ shift of the peak in the photoluminescence spectra confirms the presence of an integrated electric field in (111)A-heterostructures caused by the piezoelectric effect. It is shown that (100)-heterostructures generate a THz signal of approximately the same level (the scatter of THz field amplitude values is no more than 30% of the average value) regardless of strain, while in a series of (111)A-heterostructures the THz signal significantly increases (by 75−90%) for highly strained samples.

Keywords: molecular beam epitaxy, GaAs, InGaAs, piezoelectric effect, terahertz emission, femtosecond laser.

DOI: 10.61011/EOS.2025.03.61153.138-24

Introduction

When femtosecond optical laser pulses interact with semiconductors of the type $A^{III}B^{V}$ (mainly arsenides), electromagnetic pulses with a wide frequency spectrum from sub-THz to few terahertz are generated due to bursts of photocurrent, as well as various nonlinear optical effects, whose contributions depend on the wavelength and power of photoexcitation [1]. Two conditions should be met for efficient generation of THz pulses by the photoconductivity mechanism: 1) the energy of optical pump photons should slightly exceed the bandgap of the semiconductor, 2) the lifetime of photoexcited charge carriers in the semiconductor is subpicosecond. One method to achieve short carrier lifetimes in gallium arsenide involves creating a sufficiently high concentration of point defects As_{Ga} (an As atom at a Ga lattice site), which form deep donor levels that trap photoelectrons. The high concentration of defects As_{Ga}, in turn, is achieved by the low temperature of GaAs growth (low-temperature-grown GaAs, LTG-GaAs), at which arsenic, arriving on the surface of the growing GaAs film in the form of molecules As_4 in excess, does not have time to desorb from it and is incorporated into the crystal lattice in the form of non-stoichiometric excess arsenic (including in the form of As_{Ga}).

Short-lived photoexcited charge carriers are driven by the electric field, resulting in picosecond current pulses in the film, causing THz oscillations of the electromagnetic field in the surrounding space. The electric field can be caused by the spatial separation of photoelectrons and photoholes locally formed in the pump spot region due to their different diffusion coefficient (this is the Dembert effect [2]). Also, the electric field that supports the current pulses may be embedded in the crystal; the built-in electric field may be produced by the piezo effect.

Semiconductors with the above properties are the basis for the fabrication of photoconductive antennas (PCA). Such antennas are sources and detectors of THz radiation, in which the electric field is provided by the bias applied to the electrodes. However, alternative THz sources are also studied: femtosecond laser irradiated surfaces of semiconductor films without electric bias, among which the highest efficiency is noted for *p*-InAs [3]. From a practical standpoint (for developing commercial time-resolved THz spectroscopy systems based on photoconductive antennas), photoexcitation is conveniently achieved using a femtosecond fiber laser with a wavelength of $1.56\,\mu$m [4,5]. A suitable bandgap is offered by the solid solution $In_xGa_{1-x}As$ ($x > 0.5$), which has a well-established epitaxial growth technology for producing crystallographically perfect thin films. Heterostructures with alternating thin layers of $\{In_xGa_{1-x}As/In_xAl_{1-x}As\}$ ($x > 0.5$) are also suitable for $1.56\,\mu$m pumping. They offer a significant advantage over bulk $In_xGa_{1-x}As$ films due to their substantially higher dark resistance [6]. Efficient photoconductive antennas manufactured on the base of {InGaAs/InAlAs} multilayer heterostructures were reported in [7,8,9].

A uniform polarization **P** due to the piezoelectric effect is established in the elastically stressed epitaxial layers of $In_xGa_{1-x}As$ or $In_xAl_{1-x}As$. In layers epitaxially grown on a substrate with (111) orientation, the piezoelectric polarization vector is directed along the growth axis [111], i.e., perpendicular to the heterostructure plane. Two-dimensional charge layers that create a vertical electric field are formed at the boundaries between the epitaxial layers of $In_xGa_{1-x}As$ and $In_xAl_{1-x}As$ due to the polarization gap div **P**. This field depends on the elastic deformation of the strained layer, determined by the In mole fraction in it, and does not depend on the layer thickness.

Low-temperature epitaxial growth, on the one hand, facilitates the formation of point defects of As_{Ga}, which are functional from the point of view of THz generation, on the other hand, it leads to the formation of undesirable defects — small-angle mosaic blocks, twins, packing defects, and even polycrystalline regions in a single-crystal film, and when non-singular substrate (111)A is used, the film grown at reduced temperature contains more such defects and can even become completely polycrystalline (this also depends on the ratio of fluxes of elements of groups V and III) [10]. The above listed undesirable defects reduce the mobility of photoexcited charge carriers and also cause partial relaxation of elastically stressed layers and reduction of the built-in electric field because of the piezo effect. Therefore, during the epitaxial growth of pseudomorphic quantum wells, a compromise must be sought between the concentration of point defects of As_{Ga} and the degree of single crystallinity by selecting an intermediate growth temperature.

The aim of the present study is to utilize built-in electric fields to enhance the efficiency of THz electromagnetic oscillation generation by the surface of multilayer semiconductor heterostructures of $\{In_xGa_{1-x}As/In_xAl_{1-x}As\}$ under the action of femtosecond optical pumping.

Internal electric field modeling

To evaluate the influence of the built-in electric field (caused by the piezoelectric effect) on the electron and hole states in strained superlattices[1] {InGaAs/InAlAs} on InP substrates, the band structure was numerically simulated in Nextnano software. The Schrödinger equation was solved in the effective mass approximation for electrons and heavy holes. The wave functions and charge carrier energies were calculated as a function of the thickness and composition of the $In_xGa_{1-x}As$ and $In_xAl_{1-x}As$ layers. The optical transition energy was determined based on these data. The Poisson equation was additionally solved for (111)-oriented layers to determine the electrostatic potential created by the piezoelectric charges.

[1] Here, the term „superlattice“ is used not in the strict sense but more broadly to denote a periodic sequence of semiconductor layers (not necessarily thin) that does not imply the coupling of energy levels from adjacent quantum wells into a unified band spectrum [11]. „Heterostructures with multiple quantum wells“ would be a more unambiguous, but also more cumbersome description.

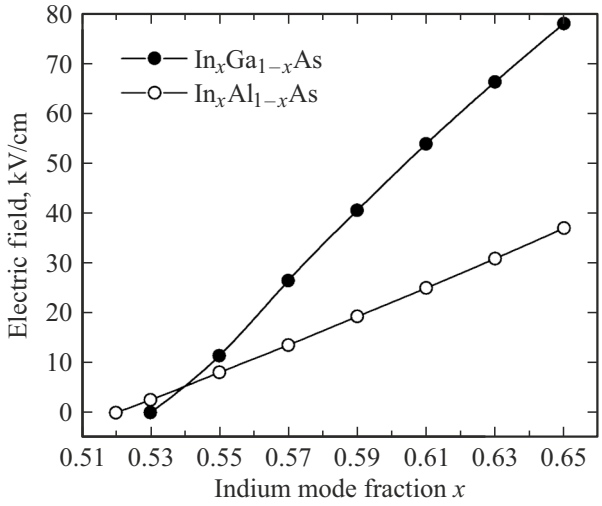

Figure 1. Calculated dependence of the built-in electric field strength on mole fraction of indium x in strained layers of $In_xGa_{1-x}As$ and $In_xAl_{1-x}As$ with orientation (111) on InP substrate.

The calculated dependence of the integrated electric field formed in the $In_xGa_{1-x}As$ (111) layer grown on InP substrate on the indium mole fraction x is shown in Fig. 1. Hereinafter, it was assumed that the $In_xGa_{1-x}As$ layer is completely unrelaxed at any value of x, in view of which it is possible to employ the Hooke's formulas to relate mechanical strain and stress. It can be seen from Fig. 1 that there is no built-in field at $x = 0.53$ when the lattice parameters of $In_xGa_{1-x}As$ and InP coincide. The buillt-in field in the $In_xGa_{1-x}As$ layer increases with x, which is attributable to the increase of the difference between the lattice parameters of $In_xGa_{1-x}As$ and InP. When $x = 0.7$, the built-in field strength is ~ 100 kV/cm.

The dependence of the built-in electric field on the composition x in $In_xAl_{1-x}As$ layers has a similar character, but the amplitude of the field strength is smaller compared to $In_xG_{1-x}As$ by about 2 times at the same values of elastic strain due to smaller values of piezoelectric coefficients. There is no electric field when $x = 0.52$. When x deviates from 0.52, the lattice parameter of $In_xAl_{1-x}As$ becomes different from the lattice parameter of the InP substrate and an built-in electric field appears, the sign of which depends on the sign of the difference $(a_{InAlAs} - a_{InP})$.

For real heterostructures, it is necessary to consider the critical thicknesses of $In_xGa_{1-x}As$ and $In_xAl_{1-x}As$ layers, which depends on the composition x. To maximize the influence of the piezoelectric field on both the charge carrier transport dynamics and the semiconductor band structure, it is necessary to increase the electric field localization region — i.e., the thickness of the strained epitaxial layers. However, the accumulation of elastic strains in the strained layers of $In_xGa_{1-x}As$ and $In_xAl_{1-x}As$ with the increase of thickness may lead to plastic relaxation, which will deteriorate the crystalline perfection of the layers as well

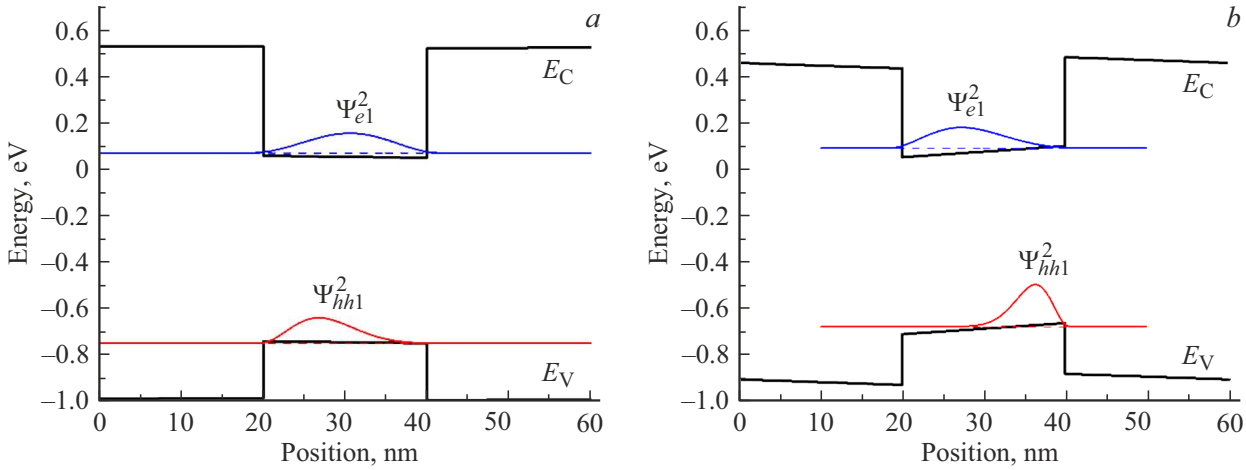

Figure 2. Band diagrams of (111)-oriented superlattices $In_{0.53+\Delta x}Ga_{0.47-\Delta x}As/In_{0.52-\Delta x}Al_{0.48+\Delta x}As$: $\Delta x = 0$ (*a*), 0.07 (*b*).

as reduce the built-in field. Therefore, the thicknesses of $In_xGa_{1-x}As$ and $In_xAl_{1-x}As$ layers in the superlattice are chosen to be sufficiently large in this paper but they are smaller than the corresponding critical values.

Lattice-matched heterostructures $\{In_{0.53}Ga_{0.47}As/In_{0.52}Al_{0.48}As\}$ are used as reference samples, where the lattice parameter matches that of the InP substrate. The compositions of $In_xGa_{1-x}As$ and $In_xAl_{1-x}As$ layers are modified to generate the vertical piezoelectric field. Intentional reduction of In content in $In_xGa_{1-x}As$ layers is undesirable because it increases the width of the band gap and will make impossible the photoexcitation of such heterostructures by a 1.5 μm laser. Therefore, the mole fraction of indium x in the $In_{0.53+\Delta x}Ga_{0.47-\Delta x}As$ layers was increased by $\Delta x = 0.07$ and 0.12. If the average lattice parameter of the heterostructure is equal to the lattice parameter of the substrate, the elastic strain will not accumulate during the growth process of the heterostructure. For this purpose, the mole fraction of indium x in the barrier layers of $In_{0.52-\Delta x}Al_{0.48+\Delta x}As$ decreased by the same values of $\Delta x = 0.07$ and 0.12. Such structures are called lattice-compensated structures, and they are used to grow large numbers of strained epitaxial layers without plastic relaxation.

Band structure simulations were performed using the Nextnano software to evaluate the effect of the built-in electric field on electron and hole states in (111)-oriented $\{In_xGa_{1-x}As/In_xAl_{1-x}As\}$ superlattices. The results of simulation of two heterostructures with quantum well (QW) $In_xGa_{1-x}As$ with a thickness of 20 nm are shown in Fig. 2. $In_xGa_{1-x}As$ and $In_xAl_{1-x}As$ layers are consistent with the substrate in terms of lattice parameter in the first heterostructure, and a lattice-compensated mismatch $\Delta x = \pm 0.07$ is introduced in the second heterostructure.

The band profile is rectangular for both electrons and holes in the heterostructure without elastic strain. The depth of the QW is determined by the energy band gaps at the boundary $In_xGa_{1-x}As/In_xAl_{1-x}As$. The built-in electric field „tilts“ the conduction band and valence band in an elastically stressed heterostructure. It should be noted that due to the opposite signs of elastic strain in $In_xGa_{1-x}As$ layers (experiencing compression) and $In_xAl_{1-x}As$ layers (experiencing tension), the electric fields in these layers are oppositely directed.

The potential in the $In_xGa_{1-x}As$ layer becomes quasi-triangular as a result of the built-in electric field. This potential stretches electrons and holes to opposite sides of the $In_xGa_{1-x}As$ layer and pushes charge carriers to the $In_xAl_{1-x}As$ barrier layers. The electric field reduces the overlap of wave functions of electrons and holes in the QW, and simultaneously reduces the energy of optical transitions between the electron and hole quantized energy subbands (quantum-confined Stark effect). This effect leads to the experimentally observed shift of the peak from QW on the photoluminescence spectrum to the red side [12,13,14].

The optical transition energy $e1-hh1$ is 0.821 eV for a lattice-matched $In_{0.53}Ga_{0.47}As/ In_{0.52}Al_{0.48}As$ QW with a thickness of 20 nm, and it should not depend on the substrate orientation. The optical transition energy shift will be 0.767 eV (100) → 0.736 eV (111)A for $In_{0.60}Ga_{0.40}As/In_{0.45}Al_{0.55}As$ QW with a thickness of 20 nm; the optical transition energy shift will be 0.729 eV (100) → 0.665 eV (111)A for $In_{0.65}Ga_{0.35}As/In_{0.40}Al_{0.60}As$ with a thickness of 20 nm.

Samples and research methods

Based on the simulation results of the band structure and the integrated electric field, we proposed the design of strained (pseudomorphic) heterostructures: each sample is an unalloyed 25-period superlattice with a nominal composition of $In_{0.53+\Delta x}Ga_{0.47-\Delta x}As$ and $In_{0.52-\Delta x}Al_{0.48+\Delta x}As$ layers, separated from the InP substrate by a buffer layer of $In_{0.52-\Delta y}Al_{0.48+\Delta y}As$, where Δx and Δy is the

Table 1. Epitaxial growth parameters of heterostructures InP/buffer $In_{0.52-\Delta y}Al_{0.48+\Delta y}As$ / superlattice $\{In_{0.53+\Delta x}Ga_{0.47-\Delta x}As$ / $In_{0.52-\Delta x}Al_{0.48+\Delta x}As\}\times 25$ (T_g is the growth temperature, γ is the ratio of the pressure As_4 to the pressure of elements of group III group, v is the growth rate) and electron transport parameters (n_{2D} is the two-dimensional electron concentration, μ is the electron mobility)

№	Substrate orientation	Δx	Δy	v_{InGaAs}, Å/min	γ_1	v_{InAlAs}, Å/min	γ_2	n_{2D}, 10^{12} cm^{-2}	μ, cm^2/(V·s)
114	(100)	0	0	128	31	130	33	0.05	3310
115	(111)A			128	31	130	33	0.23	86
120	(100)	0.07	0	78	41	103	45	0.30	3940
121	(111)A			78	41	103	45	1.65	59
116	(100)	0.07	0.07	100	31	133	32	0.20	3670
117	(111)A			100	31	133	32	0.84	97
118	(100)	0.12	0	72	40	116	39	0.34	3610
119	(111)A			72	40	116	39	1.17	78

$In_{0.53+\Delta x}Ga_{0.47-\Delta x}As$	10 nm	Protective layer
$In_{0.52-\Delta x}Al_{0.48+\Delta x}As$	20 nm	×25
$In_{0.53+\Delta x}Ga_{0.47-\Delta x}As$	20 nm	
$In_{0.52+\Delta y}Al_{0.48+\Delta y}As$	300 nm	Buffer
InP (100) or (111)A	–	Substrate

Figure 3. Generalized design of samples with multiple QWs.

deviation of the indium mole fraction from the lattice-matched compositions $In_{0.53}Ga_{0.47}As$ (for quantum wells) and $InIn_{0.52}Al_{0.48}As$ (for the bottom 300 nm buffer layer) relative to the InP substrate, respectively. The thickness of the superlattice layers (20 nm) is chosen such that it does not exceed the critical value, so that the elastic stresses in the layer do not relax and the layer remains pseudomorphic. The heterostructures are categorized into 4 types: lattice-matched with InP substrate ($\Delta x = \Delta y = 0$), heterostructures with mismatched superlattice ($\Delta x = 0.07$, $\Delta y = 0$), heterostructures with mismatched superlattice and mismatched buffer ($\Delta x = 0.07$, $\Delta y = 0.07$), heterostructures with strongly mismatched superlattice ($\Delta x = 0.12$, $\Delta y = 0$). The main role of the buffer is the reduction of the defect concentration in case of the transition from substrate to superlattice, but in our case, the mismatched buffer $In_{0.45}Al_{0.55}As$ also plays the role of an insulating layer due to the larger bandgap width compared to the substrate InP: 1.34 and 1.64 eV at room temperature, respectively [15]. Such an insulating layer may be of considerable importance for the studied photoconductive heterostructures, which suffer from lower specific dark resistance compared to GaAs. Moreover, the mismatched buffer inevitably introduces a small additional elastic stress into the overlying superlattice and thus may affect the built-in field formed therein. The design of the heterostructures is shown in Fig. 3.

Heterostructures of the proposed design were synthesized by molecular beam epitaxy (MBE) in a CNA-24 setup on semi-insulating InP substrates with crystallographic surface orientations of (100) and (111)A, each heterostructure design was realized on substrates with both orientations. Before each process in the growth chamber, pre-growth preparation of the substrates was performed in a flux of As_4 at a temperature of 530°C for 15 min. All layers were grown at a temperature of $T_g = 350$°C. The value of growth temperature T_g was monitored using a thermocouple integrated in the sample holder, and the values of partial pressures P_{As_4}, P_{Al}, $P_{Ga}$and P_{In} were monitored using a retractable Alpert–Bayard sensor. Specific values of γ which is the flux ratios of the elements of group V (As_4) and III group (Al + Ga + In) were chosen empirically based on the average values of γ which are optimal for growth on substrates with this orientation. Growth parameters varying for different samples are listed in Table 1.

The built-in electric fields in the grown samples were evaluated by photoluminescence (PL) spectroscopy, which allows determining the field-induced energy shift of interband optical transitions in superlattices (quantum Stark effect). The measured samples were held in an optical cryostat at a temperature of 77 K. Photoluminescence was excited by radiation from a solid-state laser with wavelength 532 nm focused on the sample surface into a spot of size $\sim 150\,\mu$m and power density ~ 1900 W/cm^2. The PL signal in the region of 1.2–2.0 eV was detected by a liquid nitrogen-cooled FEM-62 photomultiplier tube, and the PL signal in the region of 0.6–1.2 eV was detected by uncooled InGaAs pin-photodiode Hamamatsu using the synchronous detection technique.

The electrophysical parameters (conductivity type, concentration and mobility of charge carriers) were measured using the four-terminal van der Pauw method.

The actual layer composition and period thickness of the grown superlattices were clarified by high-resolution X-ray diffractometry. The diffraction reflectance curves from

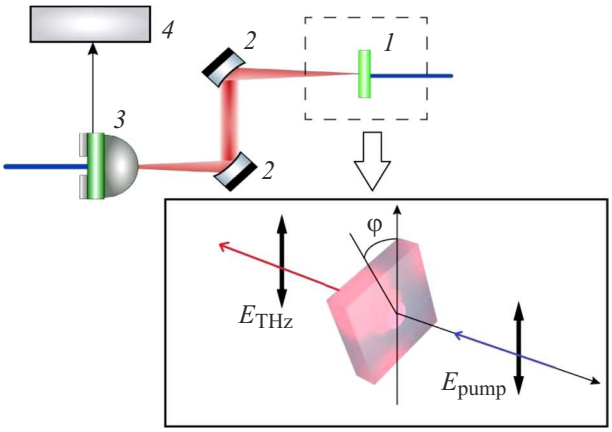

Figure 4. Principal schematic diagram of a time-resolved THz spectroscopy setup: *1* is the sample, *2* are the parabolic mirrors, *3* is the PCA detector integrated with a silicon lens, *4* is the synchronous detector.

the samples were measured using Ultima IV diffractometer (Rigaku) with radiation of copper tube Cu K_α (30 kV, 30 mA, $\lambda = 1.54056$ Å), and Ge (220)×2 crystal was used as a monochromator.

The generation of THz oscillations in the samples was studied using a time-resolved THz spectroscopy setup; the schematic diagram of the setup is shown in Fig. 4. The source of linearly polarized optical pumping was a fiber Er^{3+} laser with a wavelength of 1550 nm, a pulse duration of 100 fs, and a repetition rate of 70 MHz. After passing through the focusing lens and beam splitter, a portion of the radiation with an average power of 20 mW was driven through a system of mirrors to the PCA detector (commercial PCA Menlo Systems). The main beam with an average power of 100 mW (individual pulse energy 1.4 nJ) was directed to a controlled delay line, then to a mechanical beam modulator rotating at a frequency of 2.3 kHz, and then incident normal to the test sample. The specimen could rotate by angle φ around an axis coincident with the normal to the surface (inset in fig. 4). The THz radiation generated in the sample in the pump direction was collected by a pair of parabolic mirrors and focused by a silicon lens integrated with the PCA detector. The PCA detector was rotated for the best detection of the THz radiation, assuming that the THz radiation is also linearly polarized and its polarization coincides with the pump polarization. The THz-modulated photocurrent in the PCA detector was detected by a synchronous detector, and as a result, the time profile of the THz wave field strength at various time points after the arrival of the pump pulse, i.e. the waveform of the THz pulse, was measured.

Electron transport and photoluminescence

The measured values of the concentration and mobility of charge carriers are summarized in Table 1. Electrons are main charge carriers in all samples. When the substrate (100) is replaced by the substrate (111)A, the electron mobility sharply drops and their concentration significantly increases (by 3.5–5.4 times). This can be explained by the formation of a large number of extended defects that scatter electrons, as well as point defects of donor type that form energy levels in the upper part of the band gap. A trend of the increase of the electron concentration with the increase of Δx is noticed, which is explained by the increase of electron confinement in the deeper QW. However, this smooth trend is interrupted in a row of (111)A samples and it is masked by a much sharper increase of the electron concentration in sample № 121 with an intermediate composition. It should be noted that layers of sample № 121 were grown at the lowest speed and at the highest values of the ratio of fluxes of elements V/III. It is possible that these differences in growth conditions result in the formation of an increased concentration of some point defects active as donors. In this case, the electrons in sample № 121 should experience strong scattering, which is confirmed by the measured mobility value, which is minimal in the row of (111)A-samples.

The PL spectra of the studied heterostructures are shown in Fig. 5. The photoluminescence of samples on InP (100) substrates is significantly more intense than the PL of samples on InP (111)A substrates. For this reason, the signal-to-noise ratio of the (100)-samples is substantially higher, and two peaks are confidently observed on the spectra (in the explicit form for samples № 116, 118, 120, as a peak with „arm“ for sample № 114). These spectra are approximated by two Gaussians; the positions of the centers of the Gaussians are given in Table 2. The spectra of samples № 116, 118, 120 have a general shape: the left (long-wave) peak is less intense and less broad, its half-width is in the range of 0.015–0.019 eV; the right (short-wave) peak is more intense and broader, its half-width is 0.043–0.044 eV; the area of the right Gaussian is 6–10 times the area of the left one. The PL spectrum of the sample № 114 differs in that its constituent Gaussians have opposite characteristics: the long-wavelength peak is broader and more intense, while the short-wavelength peak is narrower and weaker. The presence of two components in the PL spectra is explained by the formation of two energy levels in these QW. Both peaks are shifted to the red side in the series of (100)-samples № 114 → 120 → 116 → 118, the maximum shift of the first peak is 0.08 eV. This suggests that in spite of the identical nominal composition of samples № 120 and 116, in reality the core of sample № 116 could be formed deeper due to the increase of Δx. Generally, the discussed spectra exhibit the following unambiguous trend: an increase of the mismatch of the heterostructure (sample № 114 → 120 → 116 → 118) is accompanied by a decrease of the PL intensity.

The photoluminescence of (111)A samples is much less intense and the signal-to-noise ratio is smaller. Only a single peak can be distinguished on the PL spectra, the parameters of which are given in Table 2. The

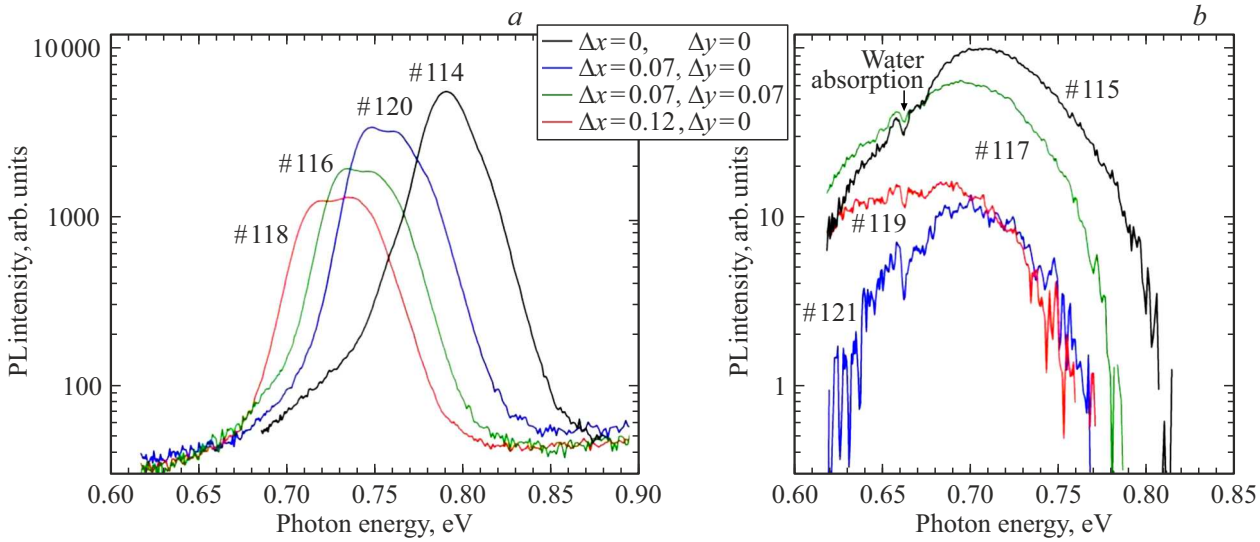

Figure 5. PL spectra of superlattice heterostructures InP/buffer $In_{0.52-\Delta y}Al_{0.48+\Delta y}As$/ superlattice $\{In_{0.53+\Delta x}Ga_{0.47-\Delta x}As/In_{0.52-\Delta x}Al_{0.48+\Delta x}As\} \times 25$ measured at 77 K: (*a*) samples on InP (100) substrates, (*b*) samples on InP (111)A substrates.

Table 2. Theoretical and experimental values of the energy of optical transitions in CNTs

Sample	Δx	Δy	$e1-hh1$, eV		$e2-hh1$, eV	Stark shift $\Delta\hbar\omega$ ($e1-hh1$), meV	
			Theory	Experiment		Theory	Experiment
114	0	0	0.821	0.791	0.820	0	85 ± 2
115			0.821	0.706 ± 0.002	–		
120	0.07	0	0.767	0.744	0.760	31	46 ± 5
121			0.736	0.698 ± 0.005	–		
116	0.07	0.07	0.767	0.729	0.746	31	34 ± 2
117			0.736	0.695 ± 0.002	–		
118	0.12	0	0.729	0.712	0.735	64	42 ± 10
119			0.665	0.670 ± 0.010	–		

absorption of the PL-signal by water vapor, which distorts the shape of the weak peak, makes it particularly difficult to determine the optical transition energy for the sample № 119. The weak PL of these samples can be explained by the increased role of radiation-free recombination of photoexcited charge carriers on point defects formed during epitaxial growth on InP (111)A substrates. The peak shifts to the red with the increase of IFx14xxE, but the maximum shift 0.02–0.03 eV is smaller than in the series of (100)-samples. The correlation between the PL intensity of the samples considered and their mismatch with the substrate is also present as in the previous case, but less unambiguous.

The difference in the observed PL energies of optical transitions in compositionally similar (100)- and (111)A-samples indicates the presence of a built-in field in (111)A-samples. For the pair of samples № 114 and 115, the shift of the PL peak indicates that these samples are not actually lattice-matched with the substrate, because in lattice-matched heterostructures there are no conditions for the manifestation of the piezo effect. Analysis of the diffraction reflection curve showed that the real composition of superlattices № 114 and 115 is as follows: $\{In_{0.58}Ga_{0.42}As$ (22.2 nm)/$In_{0.52}Al_{0.48}As$ (26.0 nm)$\}$, i.e. they are indeed markedly mismatched with the InP substrate. The built-in field strength in the sample № 115 should be ~ 30 kV/cm in the QW at $x = 0.58$. Further, by comparing the observed shift of the PL peak with the theoretically predicted shift for the other pairs of samples (and also by specifying the composition relative to the nominal one based on the position of the PL peak), we can estimate the built-in field: the real field strength in samples № 121 and 117 is close to the expected field strength and is ~ 70 kV/cm, while in sample № 119, the field is about 2/3 of the expected value

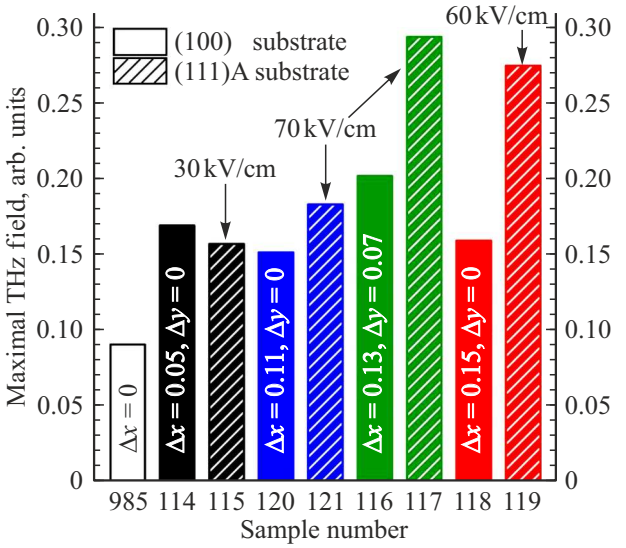

Figure 6. Comparative efficiency of THz generation of the studied samples (values of indium mole fraction in the QW $x = 0.53 + \Delta x$ and in the buffer $y = 0.52 - \Delta y$, refined by X-ray diffractometry and spectroscopy PL are indicated).

of ~ 60 kV/cm. The weakening of the built-in field must be attributable to partial relaxation of elastic stresses through dislocation formation.

Generation of THz radiation

Fig. 6 shows the values of the effective amplitude of the THz field strength generated by the samples in a convenient form for comparison (the effective amplitude was defined as the maximum value of „spread" in the wave form of THz field strength oscillations). In addition, the sample № 985 (100), which comprises a 1.2 μm thick LTG-$In_{0.53}Ga_{0.47}As$ layer grown at temperature of 200°C on an InP (100) substrate [16]. It was found that a pair of samples with weakly mismatched layers (№ 114 and 115) have almost the same efficiency of radiation (the difference in the amplitude values of THz oscillations is less than 8%), and in each pair of samples with mismatched and strongly mismatched layers (№ 120–121, № 116–117, № 118–119) the heterostructure on (111)A substrate generates THz radiation more efficiently than the analogous heterostructure on the standard (100) substrate. It can be observed that the amplitude of the THz field strength generated by samples on standard substrates is at about the same level, while for samples on (111)A-substrates, the amplitude generally increases with the increase of the layer mismatch, and hence with the increase of the elastic stresses in multiple QW. Thus, the increase of the mismatch of layers (and therefore the increase of the built-in field in the (111)A-samples) results in the increase of the ratio $E_{(111)A^{eff}}/E_{(100)^{eff}}$.

Defectivity of the crystal structure (point defects causing radiation-free recombination and dislocations by which plastic relaxation of elastic stresses occurs) has no effect on the efficiency of THz generation. If point defects are considered, it can be seen that all samples on standard (100)-substrates give a much brighter PL than all samples on (111)A-substrates, while the THz signal from them is weaker. Further, among the (111)A samples, the brightest PL is provided by the № 115 sample, and its THz signal is also the weakest. But sample № 121 with the weakest PL (hence, the one with the largest concentration of point defects) also showed a very low THz signal. The weakest THz signal among the samples on (111)A substrates is obtained from the № 115 sample with minimal elastic stresses, and thus with minimal dislocations if dislocations are taken into account.

Let us discuss the physical causes of THz emission in the studied semiconductor films. A rapidly time-varying photocurrent $J(t)$ emits electromagnetic waves, in the far field the amplitude of the waves E_{THz} is proportional to the acceleration of the charge or the time derivative of photocurrent:

$$E_{THz} \propto \frac{dJ(t)}{dt}. \quad (1)$$

The main mechanisms of THz radiation generation, providing rapidly changing photocurrent, are usually the following: Dember effect (short-lived photoexcited charge carriers are set in motion by the electric field generated in the semiconductor at its non-uniform illumination due to different diffusion coefficient of electrons and holes); built-in field effect (short-lived photoexcited charge carriers are set in motion by the field embedded in the semiconductor due to surface states or piezo effect); optical rectification of femtosecond pulses (displacement of the average position of bound electrons swung by the optical field due to the spatial asymmetry of the lattice potential for electrons, and the emergence of a constant component of the semiconductor polarization, disappearing with the termination of the femtosecond pulse) [17]. The first two effects can explain the observed THz generation at normal incidence of the pump radiation on the samples only if there is a lateral (i.e., in the film plane) component of the photocurrent or if there is a nonzero projection of oscillating dipoles onto the film plane, since otherwise the main THz radiation would propagate along the sample surface rather than normal to it and would not be registered in our experimental geometry. It is obvious that charge carriers in superlattice samples can move only within their QW without crossing the InAlAs potential barriers. Optical rectification in the case when the pump photon energy exceeds the band gap is mainly caused by displacement photocurrents [2] and may be attributable to the contribution of both quadratic and cubic processes to the polarization of the medium [10]:

$$\mathbf{J} = \hat{\sigma}^{(2)}\mathbf{EE} + \hat{\sigma}^{(3)}\mathbf{FEE}, \quad (2)$$

where $\mathbf{E}$ and $\mathbf{F}$ are optical and constant integrated electric fields, $\hat{\sigma}^{(2)}$ and $\hat{\sigma}^{(3)}$ are the second- and third-order nonlinear conductances, which determine the intensity of

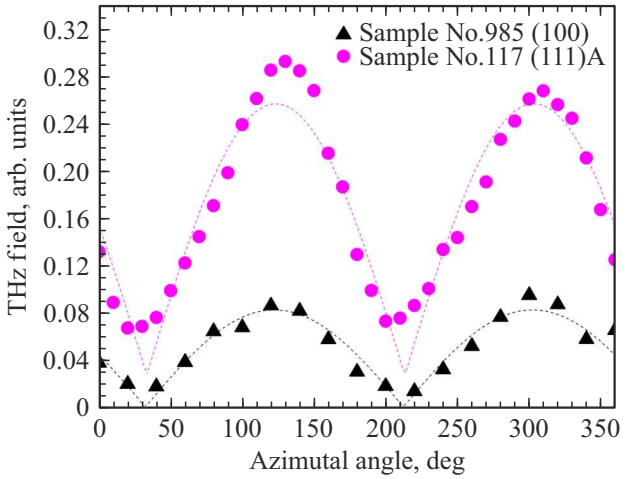

Figure 7. The dependence of the modulus of the effective amplitude of the THz signal on the azimuthal angle of rotation of the polarization plane of the pump radiation normally incident on the film surface for samples № 985 (100) and № 117 (111)A.

such nonlinear effects as optical rectification (OR) and electric field induced optical rectification (EFIOR) under the pump absorption conditions. The theory predicts the absence of EFIOR in (100)-oriented films at normal pump incidence [18], while OR is present in (100)-films but much weaker compared to (111)-films [19]. Since the measured THz generation is more efficient in (111)A samples with mismatched and highly mismatched layers, we can assume an increasing contribution of OR and EFIOR in such semiconductor films. An additional factor potentially contributing to the maximized THz signal from the pair of samples № 116 and 117 could be the presence of a compositionally sharper 30 nm $In_{0.52-\Delta y}Al_{0.48+\Delta y}As$ buffer layer in these structures. This layer enhances the reflection of the pump beam penetrating through the heterostructure, thereby promoting more efficient THz generation.

The angular dependences of the THz field distribution are closely related to the crystal symmetry and can be very informative in determining the type of nonlinear process of THz radiation generation [3]. For sample № 117 on a (111)A substrate, which exhibited the maximum THz signal, we additionally measured the dependence of the effective THz field strength amplitude on the sample's rotation angle about its normal axis in the plane perpendicular to the pump wave vector (hereafter referred to as the azimuthal angle φ). The PCA-detector did not change its orientation, remaining constantly tuned to register vertically polarized THz radiation. The azimuthal angle was counted from some initial position of the sample, which could not be associated with a specific crystallographic direction. In all cases, an inversion of the polarity of the linearly polarized THz radiation was observed when the sample was rotated by $\varphi = 180°$ (Fig. 7). For comparison, the azimuthal dependence of the THz field strength in the sample № 985 (100) is shown in the figure. It can be seen that both azimuthal dependencies exhibit a clearly defined preferred direction. However, for sample № 117, the THz field strength does not drop to zero, and a constant signal level remains present. The azimuthal dependences shown in Figure 7 can be approximated by a function of the following form

$$E_{\mathrm{THz}} = A_0 + A_1 \,|\sin(\varphi + \varphi_0)|. \qquad (3)$$

The constant, independent of the azimuthal angle component of the THz signal in this case indicates the mechanism of THz generation with the participation of transient photocurrents. The possible cause of the background signal is the capture of photoexcited carriers by deep acceptor traps with characteristic picosecond relaxation times, causing a change in the photocurrent at THz frequency under the action of the built-in field. Note that nonlinear effects can also provide a constant component of the THz signal, but only at *p*-polarization of the pump when the optical field has a non-zero projection on the normal to the film ([18], Table 1).

As is known [18], for THz generation via OR and EFIOR mechanisms in zinc-blende-type crystals, (111)-oriented films should exhibit a THz field dependence on the azimuthal angle of the form $\sin 3\varphi$, whereas (100)-oriented films show a $\sin 2\varphi$ dependence under OR (in this case, there is no EFIOR). However, we observe a dependence of the form $\sin\varphi$ after subtracting the isotropic signal. It should be noted that the sinusoid for sample № 117 is asymmetric, which is probably attributable to contributions from nonlinear processes of smaller amplitude and with a more complex angular dependence of the THz response. A similar azimuthal dependence of the form $\sin\varphi$ was observed in Ref. [20] for the THz signal from non-stoichiometric (Ga-enriched) GaAs grown on a GaAs (100) substrate, along with an azimuthally independent THz signal from a perfect GaAs (100) single crystal that vanishes at normal pump incidence. The authors explain the experimental results by the presence in nonstoichiometric GaAs of a dipole oscillating at an angle to the surface (which has a component in the plane of the film radiating along the normal) and while rigidly fixed in the crystal structure, which is strongly anisotropic due to defects. Apparently, a similar dipole generation mechanism is also dominant at low optical pumping intensities in the samples studied by us. This is indicated by the indicatrix of generation of THz radiation, which is specific for the oscillating dipole. It appears possible that at high pump intensities, the THz generation patterns may become more complex and exhibit dependencies specific to nonlinear optical processes.

The temporal form of the THz pulse field strength and the THz radiation power spectrum (without taking into account distorting over-reflections, which correspond to THz oscillations at times exceeding 20 ps), typical for all the samples studied, are shown in Fig. 8. It can be seen that the spectrum occupies the frequency band up to 1 THz, the dynamic range is 50 dB, and the maximum spectral density

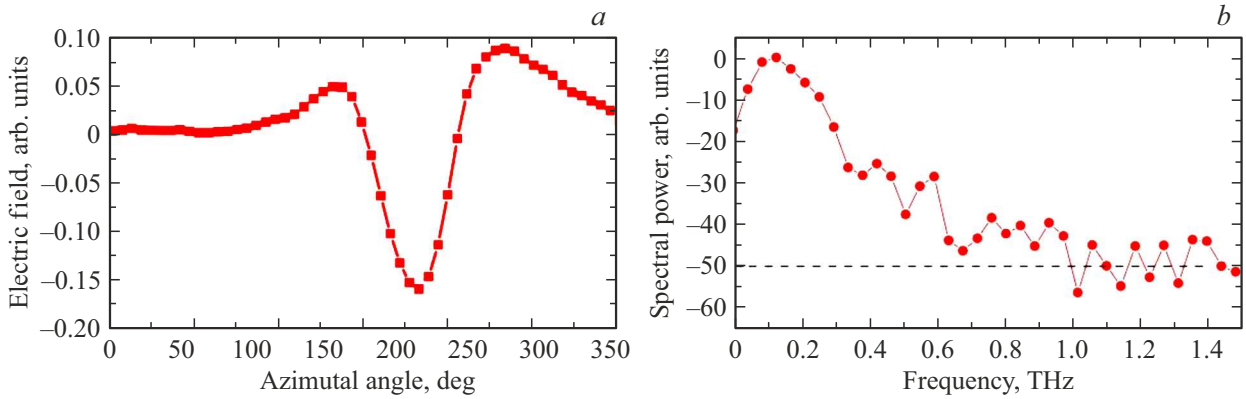

Figure 8. THz field oscillations generated by the sample № 119: (*a*) waveform, (*b*) frequency spectrum.

is observed at 130 GHz. Two water absorption lines are noticeable in the spectrum near 0.5 and 0.7 THz. Compared to results from other similar studies (e.g., [21,22,23]) on THz generation in InAs and GaAs films pumped by visible/near-IR lasers, the measured THz emission spectrum from InGaAs films is significantly narrower. This narrowing is likely attributed to the limited frequency bandwidth of the experimental setup, including the receiving antenna-detector system.

Conclusions

Heterostructures consisting of 25-period superlattices $\{In_{0.53+\Delta x}Ga_{0.47-\Delta x}As/In_{0.52-\Delta x}Al_{0.48+\Delta x}As\}$ were grown in this study by MBE method on InP substrates with (100) and (111)A orientations. The mole fraction of In in $In_{0.53+\Delta x}Ga_{0.47-\Delta x}As$ QW was gradually increased in the series of samples (and it decreased in $In_{0.52-\Delta x}Al_{0.48+\Delta x}As$ barriers). The actual compositions of the layers slightly differed from the nominal compositions and were refined by high-resolution X-ray diffractometry and PL spectroscopy. Built-in electric fields were generated in QW on InP (111)A substrates due to the piezoeffect, which caused the quantum-confined Stark effect: a decrease of the energy of inter-band optical transitions of electrons and holes between the quantized energy levels in comparison with QW on InP (100) substrates, in which the piezoeffect is not exhibited. The optical transition energy was measured by PL spectroscopy, comparison of the PL spectra of samples of the same composition on InP (100) and (111)A substrates revealed the Stark shift. Thus, the occurrence of built-in fields in (111)A-samples with strengths ranging from ~ 30 to ~ 70 kV/cm was confirmed.

The results of the experiment for the generation of THz radiation by the surface of samples under irradiation with femtosecond laser pulses (1550 nm wavelength, 100 fs pulse duration) showed that samples on InP (100) substrates generate a THz signal of approximately the same level regardless of elastic stresses, while the THz signal significantly increases in a series of (111)A samples (by about 75–90%) for highly strained samples. The difference between the experimentally observed azimuthal dependences of the THz signal of the form const + $\sin\varphi$ and those of the form $\sin 2\varphi$ and $\sin 3\varphi$, characteristic for THz generation by OR and EFIOR mechanisms, does not allow for a definitive determination of the generation mechanism, but may indicate THz generation of radiation by an oscillating dipole rigidly fixed in the crystal structure of the studied semiconductor films.

Funding

The study was supported by the grant of the Russian Science Foundation № 22-19-00656, https://rscf.ru/en/project/22-19-00656/. The epitaxial experiment was realized within the framework of the state assignment of NRC „Kurchatov Institute“.

Conflict of interest

The authors of this paper declare that they have no conflict of interest.

References

[1] D. Côté, N. Laman, H.M. van Driel. Appl. Phys. Lett., **80** (6), 905 (2002). DOI: 10.1063/1.1436530
[2] D. Cote, N. Laman, H.M. van Driel. Appl. Phys. Lett., **80**, 905 (2002).
[3] A. Krotkus. J. Phys. D: Appl. Phys., **43**, 273001 (2010). DOI: 10.1088/0022-3727/43/27/273001
[4] B. Globisch, R.J.B. Dietz, R.B. Kohlhaas, T. Göbel, M. Schell, D. Alcer, M. Semtsiv, W.T. Masselink. J. Appl. Phys., **121**, 053102 (2017). DOI: 10.1063/1.4975039
[5] *MenloSystems* [Electronic source]. URL: https://www.menlosystems.com/products/thz-time-domain-solutions/tera15-fc-3/ (date of access: 20.11.2024)
[6] Nathan M. Burford, Magda O. El-Shenawee. Opt. Eng., **56** (1), 010901 (2017). DOI: 10.1117/1.OE.56.1.010901
[7] R.J. Dietz, M. Gerhard, D. Stanze, M. Koch, B. Sartorius, M. Schell. Opt. Express, **19** (27), 25911 (2011). DOI: 10.1364/OE.19.025911

[8] A.E. Yachmenev, D.V. Lavrukhin, R.A. Khabibullin, Yu.G. Goncharov, I.E. Spector, K.I. Zaitsev, V.A. Solovyov, S.V. Ivanov, D.S. Ponomarev. Opt. i spektr., **129** (6), 741 (2021) (in Russian). DOI: 10.21883/OS.2021.06.50985.4-21
[9] D.V. Lavrukhin, A.E. Yachmenev, Y.G. Goncharov, K.I. Zaytsev, R.A. Khabibullin, A.M. Buryakov, E.D. Mishina, D.S. Ponomarev. IEEE Transactions on Terahertz Science and Technology, **11** (4), 417 (2021). DOI: 10.1109/TTHZ.2021.3079977
[10] V.L. Malevich. J. Appl. Phys., **112**, 073115 (2012).
[11] A.Y. Shik. Superlattice // The Great Russian Encyclopedia: a scientific and educational portal. URL: https://bigenc.ru/c/sverkhreshiotka-a2f3e5/?v=5490666. Date of publication: 10.11.2022.
[12] P.O. Vaccaro, M. Takahashi, K. Fujita, T. Watanabe. J. Appl. Phys., **76**, 8037 (1994). DOI: 10.1063/1.357923
[13] E.A. Khoo, J.P.R. David, J. Woodhead, R. Grey, G.J. Rees. Appl. Phys. Lett., **75**, 1929 (1999). DOI: 10.1063/1.124874
[14] A. Chin, K. Lee. Appl. Phys. Lett., **68**, 3437 (1996). DOI: 10.1063/1.115785
[15] S. Adachi. *Properties of Semiconductor Alloys: Group-IV, III–V and II–VI Semiconductors* (John Wiley & Sons Ltd., United Kingdom, 2009).
[16] G.B. Galiev, M.M. Grekhov, G.H. Kitaeva, E.A. Klimov, A.N. Klochkov, O.S. Kolentsova, V.V. Kornienko, K.A. Kuznetsov, P.P. Maltsev, S.S. Pushkarev. FTP, **51** (3), 322 (2017) (in Russian). DOI: 10.21883/FTP.2017.03.44201.8312
[17] S. Hargreaves, K. Radhanpura, R.A. Lewis. Phys. Rev. B, **80** (19), 195323 (2009).
[18] A. Krotkus. J. of Phys. D: Appl. Phys., **43** (27), 273001 (2010).
[19] M. Reid, I. V. Cravetchi, R. Fedosejevs // Phys. Rev. B, **72**, 035201 (2005).
[20] I. Beleckaitė, R. Adomavičius, R. Butkutė, V. Pačebutas, G. Molis, V. Bukauskas, A. Selskis, A. Krotkus. Electron. Lett., **52**, 1954 (2016). DOI: 10.1049/el.2016.2517
[21] P. Cicėnas, A. Geižutis, V.L. Malevich, A. Krotkus. Opt. Lett., **40** (22), 5164 (2015). DOI: 10.1364/OL.40.005164
[22] I. Nevinskas, K. Vizbaras, A. Trinkunas, R. Butkutė, A. Krotkus. Opt. Lett., **42** (13), 2615 (2017). DOI: 10.1364/OL.42.002615
[23] G.B. Galiev, S.S. Pushkarev, A.M. Buryakov, V.R. Bilyk, E.D. Mishina, E.A. Klimova, I.S. Vasilevsky, P.P. Maltsev. FTP, **51** (4), 529 (2017) (in Russian). DOI: 10.21883/FTP.2017.04.44347.8408

Translated by A.Akhtyamov